

Research Article www.acsami.org

# MXene Aerogel Derived Ultra-Active Vanadia Catalyst for Selective Conversion of Sustainable Alcohols to Base Chemicals

Niklas Oefner, Christopher E. Shuck, Leon Schumacher, Franziska Heck, Kathrin Hofmann, Jana Schmidpeter, Weigun Li, Mounib Bahri, B. Layla Mehdi, Alfons Drochner, Barbara Albert, Christian Hess, Yury Gogotsi, and Bastian J. M. Etzold\*



Cite This: ACS Appl. Mater. Interfaces 2023, 15, 16714-16722



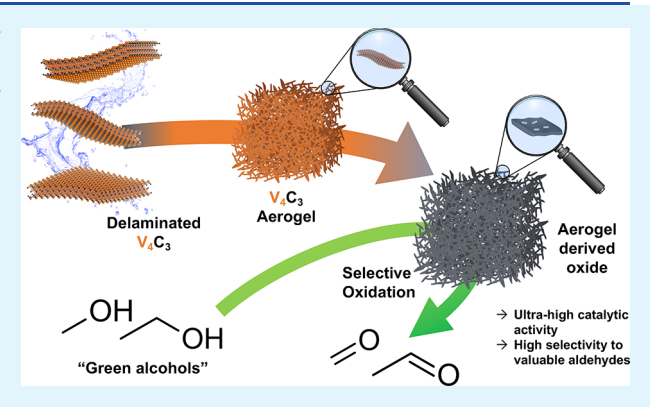
**ACCESS** 

Metrics & More

Article Recommendations

Supporting Information

ABSTRACT: Selective oxidation reactions are an important class of the current chemical industry and will be highly important for future sustainable chemical production. Especially, the selective oxidation of primary alcohols is expected to be of high future interest, as alcohols can be obtained on technical scales from biomass fermentation. The oxidation of primary alcohols produces aldehydes, which are important intermediates. While selective methanol oxidation is industrially established, the commercial catalyst suffers from deactivation. Ethanol selective oxidation is not commercialized but would give access to sustainable acetaldehyde production when using renewable ethanol. In this work, it is shown that employing 2D MXenes as building blocks allows one to design a nanostructured oxide catalyst composed of mixed valence vanadium oxides, which



outperforms on both reactions known materials by nearly an order of magnitude in activity, while showing high selectivity and stability. The study shows that the synthesis route employing 2D materials is key to obtain these attractive catalysts.  $V_4C_3T_x$  MXene structured as an aerogel precursor needs to be employed and mildly oxidized in an alcohol and oxygen atmosphere to result in the aspired nanostructured catalyst composed of mixed valence VO2, V6O13, and V3O7. Very likely, the bulk stable reduced valence state of the material together coupled with the nanorod arrangement allows for unprecedented oxygen mobility as well as active sites and results in an ultra-active catalyst.

KEYWORDS: MXenes, aerogels, heterogeneous catalysis, oxidative dehydrogenation, formaldehyde, acetaldehyde

## 1. INTRODUCTION

Oxidative dehydrogenation (ODH) of primary alcohols, like methanol and ethanol, is a highly sought after heterogeneously catalyzed gas-phase reaction. The alcohol ODH leads to the corresponding aldehydes, which are important intermediates in the chemical industry.<sup>1-4</sup> ODH of methanol is industrially applied within the FormOx process on large scales with high selectivity and an overall plant yield of 89-90%.5 However, the FormOx catalyst, an iron molybdate, suffers from deactivation, which is why the search for new, selective, active, and stable catalysts is of great interest.

The ODH of ethanol for the production of acetaldehyde is currently not applied industrially. Presently, acetaldehyde is produced in the Wacker-Hoechst process by oxidation of fossil oil-based ethylene in the aqueous phase on noble-metal catalysts containing PdCl<sub>2</sub>/CuCl<sub>2</sub>. Ethanol ODH represents a possibility to substitute fossil oil resources with ethanol as a renewable, green feedstock. It needs to be noted that ethanol is already a commodity that is produced at large scale based on renewable resources in a cost competitive manner. Due to this attractiveness, different catalyst systems have been studied for ethanol ODH. So far, the main classes of investigated catalysts have been supported metal oxides, mainly supported VO<sub>x</sub> <sup>9-13</sup> supported metal catalysts, 14,15 carbon-based catalysts, and mixed metal oxides.4,16,17

In 2011, a large class of 2D materials, MXenes, was discovered. 18 MXenes are two-dimensional transition metal carbides or nitrides with the general formula  $M_{n+1}X_nT_x$ , where M is an early transition metal, X is carbon and/or nitrogen,  $T_x$ represents the surface terminations (commonly O, OH, F, or Cl), and n = 1-4. <sup>19,20</sup> 2D MXene sheets can be processed into films, coatings or 3D macrostructures like aerogels or crumpled particles, resulting in increased specific surface area and surface accessibility.21

Received: December 18, 2022 Accepted: March 14, 2023 Published: March 24, 2023





MXenes have been explored as photocatalysts and electrocatalysts (e.g., for hydrogen evolution reaction, oxygen evolution reaction, oxygen reduction reaction), along with many other applications.<sup>22</sup> Despite their high surface area and presence of catalytically active metals in the structure, the use of MXenes in heterogeneous gas-phase catalysis is still at an early stage. Worldwide, more than 90% of all chemicals are produced using heterogeneous catalysts, which underlines the enormous importance of heterogeneously catalyzed processes and thus research on new, active, selective, and stable catalysts.<sup>23</sup> In heterogeneously catalyzed reactions, MXenes have been mostly investigated as support materials, for example, in CO oxidation, 24-28 in the conversion of methane to methanol,<sup>29</sup> or in the dehydrogenation of light alkanes.<sup>30</sup> A few MXenes, such as Ti<sub>3</sub>C<sub>2</sub>T<sub>x</sub>, Mo<sub>2</sub>CT<sub>x</sub>, and V<sub>2</sub>CT<sub>x</sub> were applied as catalysts in different reactions, including the direct dehydrogenation of ethylbenzene to styrene,<sup>31</sup> the water–gas shift reaction,<sup>32</sup> and methane dry reforming.<sup>33,34</sup>

Zhou et al. used Ti<sub>3</sub>C<sub>2</sub>T<sub>x</sub> as a precursor to produce a defectrich TiO<sub>2</sub> catalyst under ethane oxidative dehydrogenation conditions.<sup>35</sup> The Ti and oxygen vacancies in the MXene derived oxide are believed to decrease the activation energy barrier of ethane and increase the rate of reoxidation of the catalyst.<sup>35</sup> It is important to note that oxidation of MXenes allows synthesis of oxides with unusual 2D morphology that may not be achieved by other methods.<sup>36,37</sup> These studies indicate the potential for the use of MXenes as heterogeneous catalysts and as precursors to produce metal oxide catalysts with unique morphology and properties.

In general, (mixed) transition metal oxides can be regarded as important catalysts that show promising performance in methanol and ethanol ODH. Because these can be obtained from oxidation of MXene precursors, 36,38-40 the scope of this work is to study if the unique 2D properties of the precursors can lead to metal oxides with special morphology and properties in terms of defects or oxidation state of the metal, which has an enormous influence on the catalytic activity.

Herein, we synthesized V<sub>4</sub>C<sub>3</sub>T<sub>x</sub>, produced a MXene aerogel, and oxidized the aerogel to obtain a nanostructured vanadium oxide. Mild oxidation in an alcohol/oxygen atmosphere resulted in a partially oxidized vanadium oxide containing VO<sub>2</sub>, V<sub>6</sub>O<sub>13</sub>, and V<sub>3</sub>O<sub>7</sub>. This in situ activated MXene derived oxide showed outstanding catalytic activity, high selectivity toward the corresponding aldehydes, and stability for more than 10 days on stream for ODH of methanol and ethanol.

# 2. MATERIAL AND METHODS

2.1. Synthesis of V<sub>4</sub>AlC<sub>3</sub> MAX Phase. V<sub>4</sub>AlC<sub>3</sub> MAX phase was synthesized by using a mixture of vanadium (99.5%, -325 mesh, Alfa Aesar), aluminum (99.5%, -325 mesh, Alfa Aesar), and graphite (99%, -325 mesh, Alfa Aesar) powders. The powders were mixed in a 4:1.5:3 V:Al:C atomic ratio and added to a polypropylene bottle. A 2:1 mass ratio of 5 mm zirconia balls was added to this mixture. The powders were ball-milled at 60 rpm for 18 h. Afterward, the powder mixture was placed into an alumina crucible and placed into a high temperature furnace (Carbolite Gero). Ar gas was flown continually through the furnace at 200 SCCM for 1 h prior to heating and then throughout the heating/cooling process. The furnace was heated to 1500 °C for 2 h at a heating/cooling rate of 3 °C min<sup>-1</sup>. After cooling, the sintered compact was crushed with a mortar and pestle and then was placed into 9 M HCl for 24 h to dissolve residual metals and intermetallics. The powders were sieved to <40  $\mu$ m.

2.2. Synthesis of Multilayer  $V_4C_3T_x$  MXene. To synthesize V<sub>4</sub>C<sub>3</sub>T<sub>xy</sub> the V<sub>4</sub>AlC<sub>3</sub> MAX phase was slowly added to 50 wt % HF

(Acros Organics, 48-51 wt %); a ratio of 1 g of MAX to 20 mL of HF was used. Caution: Working with HF is dangerous; special safety procedures need to be followed to ensure no harm occurs to the researcher. 41 The mixture was stirred at 300 rpm at 35 °C for 96 h. Afterward, this mixture was transferred to polypropylene centrifuge tubes. Deionized (DI) water was added to the etchant solution, followed by centrifugation (10 min, 3,500 rpm). The acidic supernatant was decanted, and then, fresh DI water was added with the sediment shaken until fully redispersed. This procedure was repeated until >6 pH.

2.3. Manufacturing of the V<sub>4</sub>C<sub>3</sub>T<sub>x</sub> MXene Aerogel. 1 g of multilayer V<sub>4</sub>C<sub>3</sub>T<sub>x</sub> MXene was dispersed in 15 mL of 10 wt % tetramethylammonium hydroxide solution (Sigma-Aldrich) and stirred overnight at 35 °C and 300 rpm. The dispersion was centrifuged at 10,000 rpm until the supernatant became clear. The clear supernatant was decanted, and DI water was added to redisperse the sediment. The dispersion was centrifuged again at 10,000 rpm, and this washing step was repeated until pH 8 was reached. Once the pH was 8, the sample was redispersed again and bath-sonicated for 1 h. After centrifugation at 3,500 rpm for 10 min, the dark black supernatant was collected. This supernatant was centrifuged again at 3,500 rpm for 10 min to make sure that all multilayer MXene and MAX was removed. The supernatant was centrifuged at 10,000 rpm, and the clear supernatant was decanted and redispersed in 15 mL of DI water. The dispersion was frozen in liquid nitrogen and freezedried for 48 h using a Christ Alpha 1-2 LD.

**2.4.** Activation of the  $V_4C_3\overline{T}_x$  Aerogel. The  $V_4C_3T_x$  aerogel was activated/partially oxidized in two different ways.

2.4.1. Synthetic Air Activation (SAA). In case of synthetic air activation, the aerogel was placed between two glass wool plugs in a quartz glass reactor with an internal diameter of 4 mm. Synthetic air (20 vol % O<sub>2</sub>/80 vol % He) with a total volume flow of 20 mL min<sup>-1</sup> (STP) was fed to the reactor and heated to 300 °C for 5 h. Afterward, the reactor was cooled to room temperature in a helium atmosphere.

2.4.2. In Situ Activation (ISA). In case of the in situ activation, the aerogel was placed between two glass wool plugs in a quartz glass reactor. A mixture of 10 vol % methanol and 10 vol % O<sub>2</sub> (balance: He) with a total volume flow of 20 mL min<sup>-1</sup> (STP) was fed to the reactor and heated to 300 °C for 5 h. Afterward, the reactor was cooled to room temperature under helium flow.

2.5. Synthesis of Reference Materials. 2.5.1. Iron Molybdate. Stoichiometric Fe<sub>2</sub>(MoO<sub>4</sub>)<sub>3</sub> was prepared using a coprecipitation synthesis procedure according to ref 42. Iron nitrate nonahydrate (14.9 mmol,  $Fe(NO_3)_3$ .9  $H_2O$ , Merck,  $\geq$ 98%) and ammonium heptamolybdate tetrahydrate (22.3 mmol, (NH<sub>4</sub>)<sub>6</sub>Mo<sub>7</sub>O<sub>24</sub>·4 H<sub>2</sub>O, Merck, ≥99%) were dissolved separately in DI water (100 and 200 mL, respectively). Afterward, the aqueous iron nitrate solution was added dropwise to the molybdate solution under vigorous stirring, which instantly led to the formation of a precipitate. In order to complete the precipitation process, the solution was stirred at 100 °C for 3 h. The precipitate was isolated by filtering off and washed with DI water and ethanol (Brenntag BCD, Technical grade) before it was dried overnight at 100 °C in air. Finally, the powder was calcined in air at 500 °C for 10 h, using a corundum crucible and a tube furnace (Carbolite Gero CWF1200).

2.5.2. Vanadium Pentoxide. Bulk V<sub>2</sub>O<sub>5</sub> was purchased from Acros Organics (>99.6%).

2.5.3. Vanadium(V)oxide. Bulk VO<sub>2</sub> was purchased from Thermo Scientific Alfa Aesar (99%)

2.5.4. Supported Vanadium Oxide. For synthesis of the SBA-15 support, 4.0 g of Pluronic P123 (EO<sub>20</sub>PO<sub>70</sub>EO<sub>20</sub>, BASF) was mixed with 120 mL of 2 M HCl and 30 mL of DI water in a polypropylene bottle and stirred at 35 °C until a clear solution was obtained. Subsequently, 8.5 g of tetraethyl orthosilicate (TEOS, Sigma-Aldrich, ≥99%), which served as the precursor for SiO<sub>2</sub>, was added under stirring, which was maintained for a further 20 h at 35 °C. The bottle was placed in a furnace at 85 °C for 24 h. Afterward, the suspension was filtered by a glass frit, and the powder was calcined at 550 °C for 12 h in ambient air with a heating rate of 1.5 °C min<sup>-1</sup>. Incipient wetness impregnation was performed to load the SBA-15 with 1 V

nm $^{-2}$ . Vanadium(V) oxytriisopropoxide ( $\geq$ 97%, Sigma-Aldrich) was mixed with anhydrous 2-propanol (99.5%) in a glovebox and added to the samples while mixing in a mortar. Subsequently, the yellow powder was calcined in air at 600 °C for 12 h with a heating rate of 1.5 °C min $^{-1}$ .

**2.6. Characterization.** 2.6.1. Raman Spectroscopy. Raman spectroscopy analysis was performed at an excitation wavelength of 514.5 nm, using an argon ion gas laser (Melles Griot). The light was focused onto the sample, gathered by an optic fiber, and dispersed by a transmission spectrometer (Kaiser Optical, HLSR). The dispersed Raman radiation was subsequently detected by an electronically cooled CCD detector ( $-40\,^{\circ}$ C,  $1024\times256$  pixels). The spectral resolution was 5 cm<sup>-1</sup> with a wavelength stability of better than 0.5 cm<sup>-1</sup>. A laser power of 5 mW at the sample location was applied. Data analysis of the Raman spectra included cosmic ray removal and an auto new dark correction.

2.6.2. XPS. X-ray photoelectron spectroscopy analysis was carried out on an SSX 100 ESCA spectrometer (Surface Science Laboratories Inc.), employing a monochromatic Al K $\alpha$  X-ray source (1486.6 eV) operated at 9 kV and 10 mA; the spot size was approximately 1 mm  $\times$  0.25 mm. The base pressure of the analysis chamber was  $<10^{-8}$  Torr. Survey spectra (eight measurements) were recorded between 0 and 1100 eV with 0.5 eV resolution, whereas detailed spectra (30 measurements) were recorded with 0.05 eV resolution. To account for sample charging, the C 1s peak of ubiquitous carbon at 284.4 eV was used to correct the binding-energy shifts in the spectra. Atomic concentrations were calculated using the relative sensitivity factors (RSFs) given in Table 1.

Table 1. Relative Sensitivity Factors Used for the Calculations of Elemental Concentrations from XPS Data

	C 1s	O 1s	N 1s	F 1s	V 2p
RSF	1.00	2.50	1.68	1.33	5.48

2.6.3. Ar Physisorption. Textural properties of the  $V_4C_3T_x$  aerogel and the ISA aerogel derived oxide were studied via argon physisorption analysis at 189.3 °C using a 3Flex analyzer (Micromeritics) after degassing of the samples under vacuum at 200 °C for 18 h. Specific surface areas (SSAs) were calculated using the Brunauer–Emmett–Teller (BET) method.

2.6.4. ICP-OES. The vanadium and aluminum content in the multilayer  $V_4C_3T_x$  MXene and the produced  $V_4C_3T_x$  aerogel were determined by inductively coupled plasma optical emission spectrometry (ICP-OES). ICP-OES was carried out using a PerkinElmer OPTIMA 2000DV spectrometer. For sample preparation, the materials were dissolved in aqua regia and diluted with DI water.

2.6.5. TPO. Temperature programmed oxidation (TPO) of the  $V_4C_3T_x$  aerogel was performed using a NETZSCH STA 449 C Jupiter thermo-microbalance. The sample was placed in a corundum crucible and heated to 600  $^{\circ}\text{C}$  in synthetic air with a heating rate of 2  $^{\circ}\text{C}$  min $^{-1}$ .

2.6.6. SEM. Field emission scanning electron microscopy (SEM) images were taken using a Philips XL30 FEG electron microscope. Pictures of the  $V_4C_3T_x$  aerogel and the ISA aerogel derived oxide were taken at an acceleration voltage of 30 kV.

2.6.7. XRD. X-ray powder diffraction patterns were collected at room temperature by a Stoe StadiP powder diffractometer with Cu  $K\alpha_1$  radiation (Ge[111]-monochromator,  $\lambda=1.54060$  pm, MYTH-EN-1K detector (Dectris)) in transmission geometry. The samples were placed between two X-ray amorphous polymer films.

2.6.8. HRTEM/EELS. The samples  $(V_4C_3T_x)$  MXene Aerogel or ISA aerogel derived oxide) were ground, and the powder was dispersed onto a lacy-carbon copper grid from TedPella INC. The HRTEM images were taken using a LaB<sub>6</sub> JEOL JEM2100+ TEM in low dose conditions at 200 kV. The EELS data was collected using JEOL 2100F Cs corrected scanning transmission electron microscopy at 200 kV. The EELS spectrum imaging acquisition of the vanadium L-edge was done using a Gatan Imaging Filter GIF QuantumSE series post column filter with an energy dispersion of 0.1 eV/channel.

**2.7. Catalytic Experiments.** 2.7.1. Temperature Cycling and Long-Term ODH Experiments. The catalytic reactions were performed in a continuous flow apparatus with a quartz glass tube reactor with an internal diameter of 4 mm. The catalyst was placed between two glass wool plugs. Liquid reactants were fed to the reactor by using a two-stage saturator system, and gases were dosed by mass flow controllers. The total volume flow was 20 mL min<sup>-1</sup> (STP) with helium as inert gas. Off-gas analytic was performed by an online quadrupole mass spectrometer (GAM 400, InProcess Instruments) and an online gas chromatograph (Shimadzu GC 2010) equipped with a flame ionization detector (FID) and a thermal conductivity detector (TCD).

2.7.2. Methanol ODH. For the MeOH ODH measurements, the feed consisted of 10 vol% MeOH and 10 vol%  $O_2$ . 5 mg of the  $V_4C_3T_x$  aerogel was used and activated with the reaction mixture at 300 °C until steady-state conditions were reached (6 h). Afterward, the temperature was varied within 240–320 °C in steps of 20 °C. For the reference measurements, 25 mg of  $V_2O_5$ , 100 mg of  $Fe_2(MoO_4)_3$ , 56 mg of  $VO_x/SBA-15$ , and 100 mg of the multilayer  $V_4C_3T_x$  MXene were used.

2.7.3. Ethanol ODH. For the EtOH ODH measurements, the feed consisted of 5 vol% EtOH and 10 vol%  $O_2$ . 5 mg of the  $V_4C_3T_x$  aerogel was used and pretreated with the reaction mixture at 280 °C until steady-state conditions were reached. Afterward, the temperature was varied within 200–280 °C in steps of 20 °C. For the reference measurements, 25 mg of  $V_2O_5$ , 100 mg of  $Fe_2(MoO_4)_3$ , 56 mg of

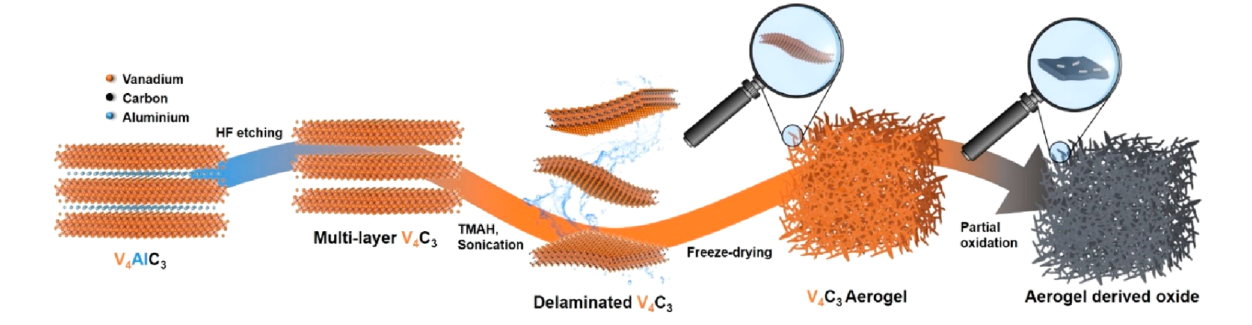


Figure 1. Schematic illustration of MXene aerogel synthesis procedure.  $V_4C_3T_x$  multilayer MXene was obtained by selective etching of the aluminum phase from the parent MAX phase  $V_4AlC_3$  with hydrofluoric acid. The multilayer MXene was delaminated in an aqueous solution using tetramethylammonium hydroxide as an intercalant and subsequent sonication. Freeze-drying of the MXene colloidal suspension led to the formation of an aerogel with a random 3D arrangement of MXene sheets. The MXene aerogel was partially oxidized to obtain the aerogel derived oxide catalyst.

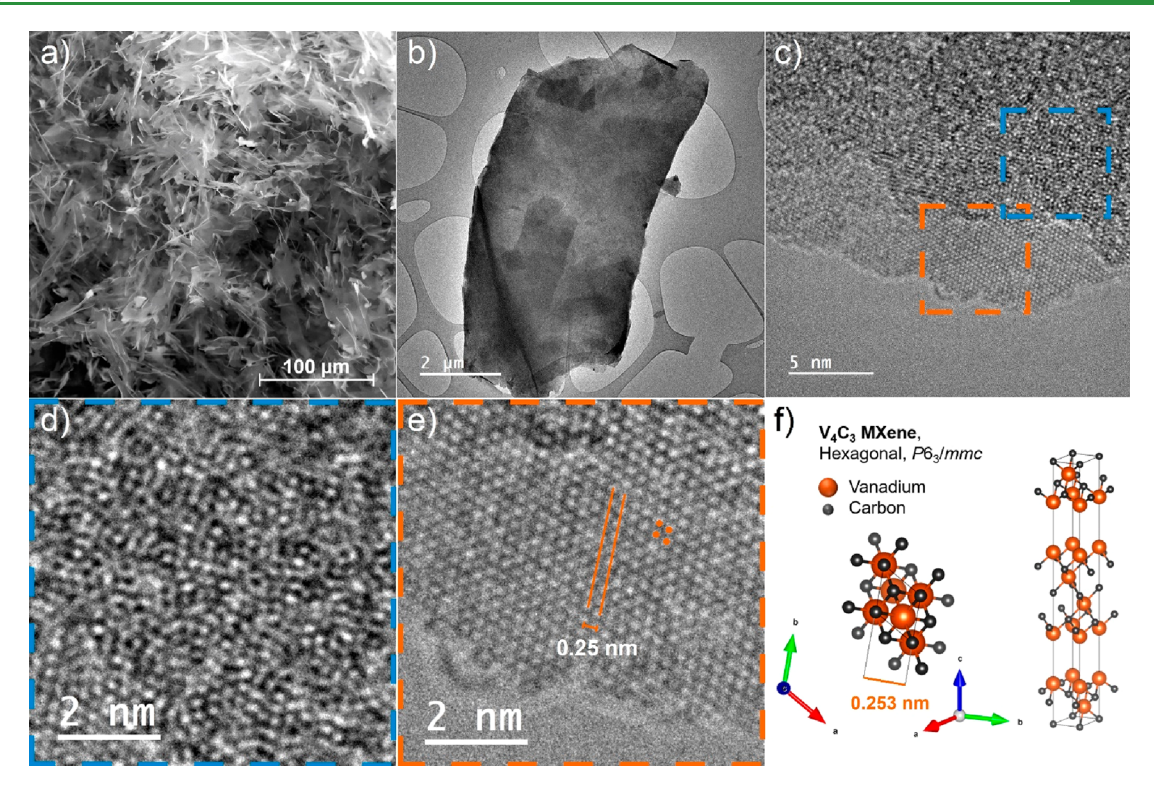


Figure 2. Characterization of  $V_4C_3T_x$  MXene aerogel. (a) SEM image of  $V_4C_3T_x$  MXene aerogel. (b) Low magnification image of a  $V_4C_3T_x$  flake. (c) HRTEM image of  $V_4C_3T_x$  showing a mixture of single and multidomain flakes. (d, e) HRTEM image multidomain area (blue) and single domain area (orange) and (f) illustration of the hexagonal MXene structure.

 ${
m VO}_x/{
m SBA}$ -15, and 100 mg of the multilayer  ${
m V}_4{
m C}_3{
m T}_x$  MXene were used.

2.7.4. Methanol and Ethanol TPD. MeOH and EtOH temperature programmed desorption (TPD) experiments were performed using the same reaction setup which was described before. 15 mg of the material was treated with 10 vol% alcohol and 10 vol% O<sub>2</sub> at 300 °C for 6 h until steady-state behavior was reached. Afterward, the temperature was lowered to 100 °C. Alcohol desorption at 100 °C was performed for 10 min (10 vol% alcohol in He). After flushing with helium for 2 h, the temperature was raised with a specific heating rate (7.5, 10, 15, and 20 °C min<sup>-1</sup>) and the off-gas was analyzed by a calibrated online mass spectrometer (GAM 400, InProcess Instruments). The total volume flow was constant at 20 mL min<sup>-1</sup> (STP).

2.7.5. Methanol and Ethanol Pulse Experiments. MeOH and EtOH pulse experiments were performed using the same reaction setup, which was described before. 15 mg of the catalyst was treated with 10 vol% alcohol and 10 vol% O<sub>2</sub> at 300 °C for 6 h until steady-state behavior was observed and then oxidized with synthetic air at 300 °C for 1 h. During the pulse experiments, the total volume flow was constant at 20 mL min<sup>-1</sup> (STP) He. Pulses were generated by an automated 6 port valve with a sample loop. By switching the 6 port valve, 50 MeOH/EtOH reduction pulses were generated. The time between the pulses was varied within 1, 2, and 3 min.

## 3. RESULTS AND DISCUSSION

**3.1. Synthesis and Characterization of V**<sub>4</sub>C<sub>3</sub>T<sub>x</sub> **Aerogel.** A simplified scheme of the synthesis procedure is shown in Figure 1. The starting material, multilayer V<sub>4</sub>C<sub>3</sub>T<sub>x</sub> MXene, was synthesized by etching the V<sub>4</sub>AlC<sub>3</sub> MAX phase with hydrofluoric acid (HF). The multilayer MXene was delaminated in aqueous solution by using tetramethylammonium hydroxide (TMAOH) as the intercalant, followed by sonication. The V<sub>4</sub>C<sub>3</sub>T<sub>x</sub> aerogel was obtained by freeze-drying the delaminated MXene dispersion. The freeze-drying step prevented restacking of the MXene sheets, leading to a random

arrangement of the sheets, resulting in a disordered 3D macrostructure, as shown in Figure 2a. Figure 2b shows a transmission electron microscopy (TEM) image of a MXene sheet. The specific surface area (SSA) was determined by argon physisorption and is calculated to be 16 m<sup>2</sup> g<sup>-1</sup> (Figure S2). Since Ar adsorbs weakly on MXenes and cannot penetrate between MXene sheets, the reported SSA is underestimated.

X-ray powder diffraction (XRD) of the aerogel (Figure S1) showed pronounced (002) and (110) reflections at  $5.2^{\circ}(2\theta)$  and  $63.5^{\circ}(2\theta)$ , respectively, confirming the existence of a  $V_4C_3T_x$  MXene. In comparison to the starting material, reflections in the  $2\theta$  region from  $35^{\circ}$  to  $45^{\circ}$  decreased significantly, indicating an increasing loss of crystallinity (or structural order) during delamination and aerogel manufacturing. Additionally, the (002) reflection of the initial MAX phase at  $7.8^{\circ}(2\theta)$  vanished, indicating a removal of the residual MAX phase. Inductively coupled plasma optical emission spectroscopy (ICP-OES) confirmed this observation by a decrease of the Al/V ratio from 0.17 in the starting material to 0.02 in the  $V_4C_3T_x$  aerogel, indicating a very low amount of residual Al in the aerogel.

The hexagonal structure of the MXene sheets was also confirmed by high-resolution transmission electron microscopy (HRTEM), as shown in Figure 2c-e. The HRTEM image of the single domain MXene (Figure 2e) clearly showed its hexagonal P6<sub>3</sub>/mmc symmetry.

The composition of the aerogel was analyzed by X-ray photoelectron spectroscopy (XPS). XPS spectra shown in Figure S3 revealed oxygen (30.5 at. %) and fluorine (9.9 at. %) surface functionalization originating from the HF etching during MXene synthesis. The V 2p XPS revealed that 54 at. % of the vanadium was bound to carbon and 46 at. % was bound

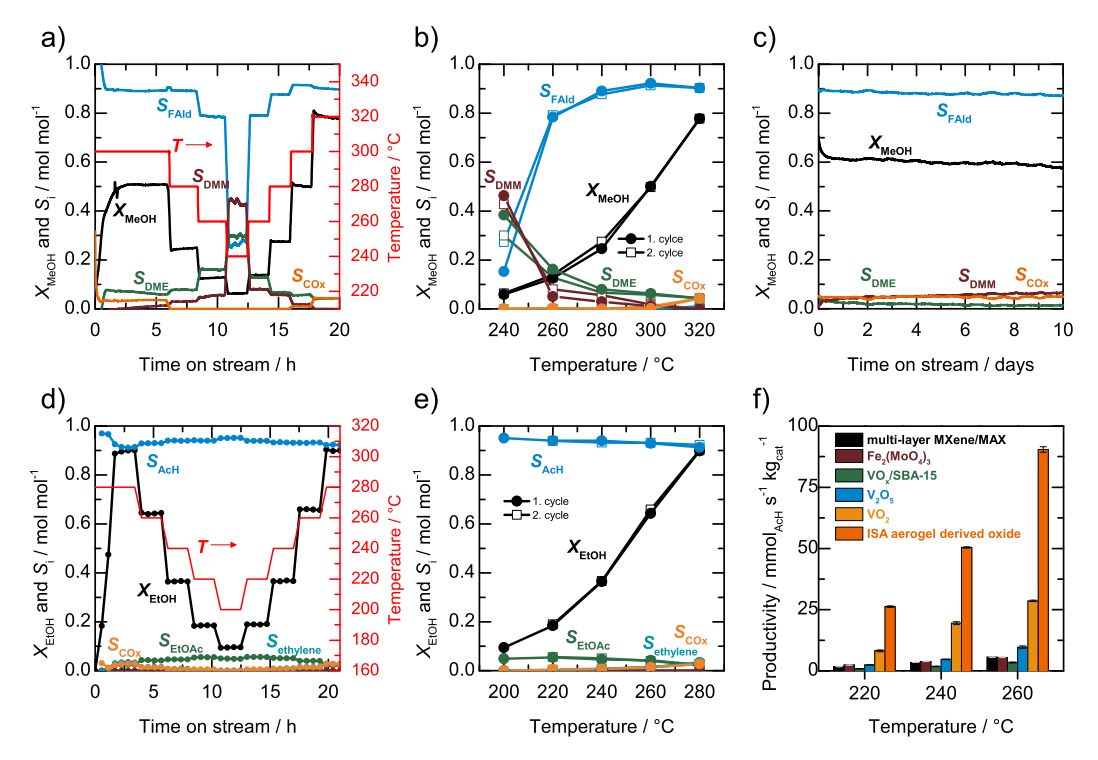


Figure 3. Methanol and ethanol ODH on *in situ* activated  $V_4C_3T_x$  aerogel derived oxide. (a) Conversion of methanol (MeOH) and selectivities to formaldehyde (FAld), dimethyl ether (DME), dimethoxymethane (DMM), and  $CO_x$  during temperature cycling against time on stream. (b) Steady-state values of conversion of methanol and selectivity to reaction products for different reaction temperatures, (c) long-term methanol ODH measurement, indicating high stability, (d) conversion of ethanol (EtOH) and selectivities to acetaldehyde (AcH), ethyl acetate (EtOAc), ethylene, and  $CO_x$  during temperature cycling against time on stream, (e) steady-state values of conversion of ethanol and selectivities to reaction products for different reaction temperatures, and (f) comparison of acetaldehyde productivity of the ISA aerogel derived catalyst compared to  $VO_2$ ,  $V_2O_5$ ,  $VO_x/SBA-15$ , and  $Fe_2(MoO_4)_3$  and the initial multilayer MXene/MAX as reference materials (error bars indicate the standard variation during the measurements).

to oxygen. The averaged oxidation state of the vanadium bound to oxygen could be determined to be +3.8.

3.2. Activation and Catalytic Performance. An oxidative treatment is necessary to convert the V<sub>4</sub>C<sub>3</sub>T<sub>x</sub> aerogel precursor into an active oxide catalyst. To study the temperature range for the oxidation of the  $V_4C_3T_x$  aerogel, temperature programmed oxidation (TPO) in synthetic air was performed (Figure S6a). The relative mass increased between 200 and 350 °C, indicating an oxidation of the aerogel in this temperature range. As these temperatures were within the range of the aimed catalytic reactions, two ways of activation of the MXene aerogel were studied: (1) the MXene aerogel was used as prepared and activated in situ under methanol ODH conditions, hence with 10 vol% methanol and 10 vol% oxygen at 300 °C (named: ISA, in situ activation), and (2) the MXene aerogel was oxidized in synthetic air at 300 °C (named: SAA, synthetic air activation) prior to testing in the ODH of methanol.

The synthetic air activation led to a highly active ODH catalyst. For methanol ODH, this resulted in a productivity to formaldehyde (FAld) of 82 mmol<sub>Fald</sub> s<sup>-1</sup> kg<sub>cat</sub><sup>-1</sup> at 300 °C (Figure S6). During temperature cycling between 240 and 320 °C, deactivation was observed at each temperature, indicating a lower catalytic stability or an induction period of the catalyst. Raman spectroscopy of the SAA aerogel derived oxide (Figure S6) revealed features of crystalline  $V_2O_5$ , indicating a high oxidation state of the material. <sup>44</sup> The XRD pattern of the SSA aerogel derived oxide is given in Figure S1 and shows weak

reflexes at  $7.5^{\circ}$ ,  $25^{\circ}$ , and  $51^{\circ}(2\theta)$  that cannot be clearly assigned to a known crystal structure.

The results for the ISA catalyst are shown in Figure 3a, which depicts the time-resolved conversion of methanol (MeOH) and the selectivities to the reaction product formaldehyde and the byproducts dimethyl ether (DME), dimethoxymethane (DMM), and CO<sub>x</sub>. In the first 3 h at 300 °C, the degree of conversion increased from 0 to 50% and then reached steady-state behavior. After 5 h, the ISA aerogel derived oxide showed an ultrahigh catalytic activity with a formaldehyde productivity of 134 mmol<sub>Fald</sub> s<sup>-1</sup> kg<sub>cat</sub><sup>-1</sup>. Besides the higher activity compared to the SAA aerogel derived oxide, the ISA aerogel derived oxide showed stable performance during temperature cycling between 240 and 320 °C.

At 240 °C, the methanol degree of conversion was 6% and the formaldehyde selectivity decreased to 26% while the dimethoxymethane selectivity and dimethyl ether selectivity increased to 43% and 34%, respectively. With increasing temperature and conversion, the selectivity to formaldehyde increased and was still 90% at 320 °C ( $X_{\rm MeOH} = 78\%$ ). Besides high selectivity, the material showed an outstanding activity of 217 mmol<sub>FAld</sub> s<sup>-1</sup> kg<sub>cat</sub><sup>-1</sup> at 320 °C. The averaged steady-state values of methanol conversion and the selectivities during the temperature cycling experiment are shown in Figure 3b and reveal that no significant temperature hysteresis was observed. Figure 3c shows the conversion and the selectivities to the reaction products for a long-term measurement with the ISA aerogel derived oxide at 320 °C. The catalyst showed only a

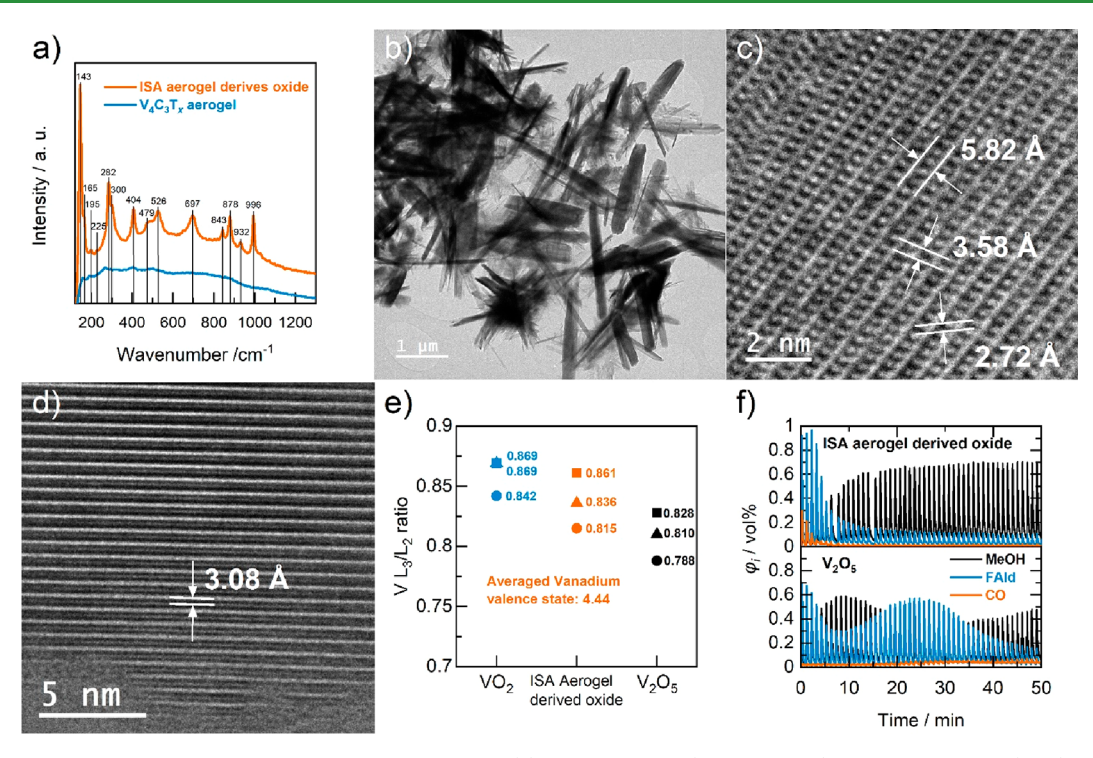


Figure 4. Post-mortem characterization of ISA aerogel derived oxide. (a) Raman spectra ( $\lambda$  = 514.5 nm) of  $V_4C_3T_x$  aerogel (blue) and ISA aerogel derived oxide (orange), (b) TEM survey image of ISA aerogel derived oxide nanorods, (c and d) HRTEM images of ISA aerogel derived oxide, indicating  $V_6O_{13}$  (c) and  $V_3O_7$  (d), (e) vanadium  $L_3/L_2$  ratios on three different spots in comparison to  $VO_2$  and  $V_2O_5$  as reference materials, and (f) volume fractions of methanol (MeOH), formaldehyde (FAld), and CO during methanol pulse experiments on the ISA aerogel derived oxide (top) and  $V_2O_5$  (bottom) with a pulse interval of 1 min.

slight decrease in degree of conversion from 63% to 58% after 10 days on stream, indicating its high stability.

Besides methanol ODH, the  $V_4C_3T_x$  aerogel was also used as catalyst precursor for ethanol ODH. To convert the aerogel to an active catalyst, the aerogel was activated *in situ* at 280 °C under ethanol ODH conditions (5 vol% ethanol, 10 vol%  $O_2$ ). The degree of conversion of ethanol (EtOH) and the selectivity to the desired product acetaldehyde (AcH) as well as the selectivities to the byproducts, ethyl acetate (EtOAc), ethylene, acetic acid (AcOH), and  $CO_x$ , against time on stream are shown in Figure 3d. After an increase of the conversion in the first 2 h, indicating active species formation, the catalyst reached steady-state behavior with a degree of conversion of 90% and an acetaldehyde selectivity of 91%.

The main side products at 280 °C were ethylene, ethyl acetate, and  $\mathrm{CO}_x$  (all around 3%). At lower temperatures, e.g., at 220 °C, and a degree of conversion of 18%, the selectivity to acetaldehyde increased to 94% and ethyl acetate became the main side product (5%). Figure 3e depicts the steady–state conversion and selectivities during temperature cycling. Again, no temperature hysteresis was observed, demonstrating the stability of the ISA aerogel derived catalyst, which also showed an outstanding acetaldehyde productivity of 123 mmol<sub>AcH</sub> s<sup>-1</sup> kg<sub>cat</sub><sup>-1</sup> at 280 °C with a yield of 83%.

Three commonly employed reference oxidation catalysts were prepared and tested to compare their performance with the MXene derived catalyst. The reference materials were bulk  $V_2O_5$ , supported  $VO_x$ , and  $Fe_2(MoO_4)_3$ , which is used as catalyst within the industrial FormOx process. Figure 3f compares the resulting mass-based productivities at different temperatures to the new ISA MXene aerogel derived oxide of this study. At all temperatures, the productivity of the new

catalyst exceeded the productivity of all reference materials by a factor of 3.2 to 16.7. Additionally, a comparison was made to a catalyst which was obtained by direct *in situ* activation of the starting precursor (multilayer MXene with residues of MAX phase) and thus without the aerogel structuring step. Here, a catalyst with an activity similar to those of the reference catalysts resulted, underpinning the importance of forming an aerogel precursor. The productivities during methanol ODH are shown in Figure S11 and show the same trend concerning the ultrahigh activity of the ISA aerogel derived oxide.

**3.3.** *Post-mortem* Characterization of ISA Aerogel Derived Oxide. After activation and temperature cycling in methanol ODH, extensive *post-mortem* characterization of the ISA aerogel derived oxide was performed to understand its high catalytic activity and to establish structure—activity relationships. The XRD pattern of the ISA aerogel derived oxide (Figure S1) showed reflections that can be assigned to metastable VO<sub>2</sub> (B) (space group C/2m). 45

VIS-Raman spectroscopy of the pristine  $V_4C_3T_x$  aerogel and the ISA aerogel derived oxide after ODH reaction was performed (Figure 4a). The pristine aerogel only showed weak Raman features at 158, 195, 263, 404, and 501 cm<sup>-1</sup>. In comparison, the ISA aerogel derived oxide showed intensive Raman bands at 996, 697, 526, 497, 404, 300, 282, 195, and 143 cm<sup>-1</sup> and additional bands at 843, 878, and 932 cm<sup>-1</sup>. Zhang et al. assigned these features to a mixture of  $VO_2$ ,  $V_6O_{13}$ , and  $V_2O_5$ . The  $VO_2$  characteristic Raman band at  $\sim$ 600 cm<sup>-1</sup> appeared to occur as an enhancement of the background in this case. It should be noted that the formation of  $V_3O_7$  could also lead to bands in the range between 840 and 940 cm<sup>-1</sup>. Since  $V_3O_7$  is not well documented, the formation of that mixed valence oxide cannot be excluded.

The ISA aerogel derived oxide was post-mortem subjected to analysis by HRTEM and electron energy loss spectroscopy (EELS). Figure 4b shows a TEM image of the ISA aerogel derived oxide, which indicated the formation of nanorods. HRTEM images of the nanorods shown in Figure 4c,d confirmed the assumption of the presence of the mixed valence oxides  $V_6O_{13}$  and  $V_3O_7$ . More HRTEM images, assigned to  $V_3O_7$  and  $V_6O_{13}$ , are shown in Figures S4 and S5. EELS analysis of three different particles was performed to estimate the averaged vanadium valence state. The  $L_3/L_2$  intensity ratios for the ISA aerogel derived oxide as well as for  $V^{4+}$  and  $V^{5+}$  references are shown in Figure 4e. The averaged oxidation state was 4.44, being in good agreement with the observations made by Raman spectroscopy and HRTEM.

The surface composition of the ISA aerogel derived oxide after ODH reaction was determined by XPS (Figure S3). In comparison to the pristine  $V_4C_3T_x$  aerogel, the ISA aerogel derived oxide had no fluorine functionalization on the surface. The O/V ratio increased from 1.72 to 2.82 after reaction, confirming oxidation of the material. Fitting the high resolution V 2p spectrum showed a decrease of carbidic vanadium from 54 to 0 at. %. The ratio of  $V_4^{4+}$  to  $V_5^{5+}$  was determined to be 0.52, in good agreement with the observation of the formation of  $V_3O_7$  ( $V_4^{4+}/V_5^{5+}=0.5$ ) or a mixture of  $V_6O_{13}$  and  $V_2O_5$  on the surface.

In summary, the MXene aerogel was *in situ* oxidized, leading to the metastable  $VO_2$  (B) phase in the bulk of the material, while the formation of  $V_6O_{13}$ ,  $V_3O_7$ , and  $V_2O_5$ , which appear either amorphous or as a thin film on the surface, could not be detected by XRD.

In addition to the detailed characterization of the ISA aerogel derived oxide, kinetic studies (including variation of oxygen concentration, alcohol concentrations, and temperature) and transient response experiments (including methanol/ethanol pulse experiments and methanol/ethanol temperature programmed desorption (TPD)) were carried out on ISA aerogel derived oxide and the less active highly oxidized bulk  $\rm V_2O_5$  to unravel the cause of the ultrahigh activity of the new catalyst.

3.4. Mechanistic Investigations of the Alcohol ODH on ISA Aerogel Derived Oxide. Kinetics of consumption of oxygen and alcohol were found to approximately follow a power-law approach. The reaction orders for methanol/ ethanol and oxygen consumption as well as the apparent activation energies for the ODH reaction on ISA aerogel derived oxide and V<sub>2</sub>O<sub>5</sub> can be found in Supplementary Section 5. In summary, slight differences in alcohol and oxygen reaction orders could be observed. The clear trend for both ODH reactions toward lower apparent activation energies for the ISA aerogel derived oxide in comparison to V<sub>2</sub>O<sub>5</sub> could be a first hint for the higher activity of the MXene aerogel derived catalyst. Methanol and ethanol TPD experiments were used to determine the activation energies of formaldehyde and acetaldehyde desorption and revealed lower desorption energies on the ISA aerogel derived oxide compared to V<sub>2</sub>O<sub>5</sub> (see Supplementary Section 6). Following the Sabatier principle, this could be a reason for the observed higher activities.

For the methanol reduction pulse experiments, a fresh ISA activated catalyst was treated at 300  $^{\circ}$ C for 1 h with 10 vol%  $O_2$  to generate a defined oxidized surface (Figure S16). 50 methanol reduction pulses in helium were applied, and the offgas was analyzed by a calibrated online mass spectrometer (see

Figure 4f). The ISA aerogel derived oxide showed full conversion of methanol in the first four pulses, mainly producing formaldehyde and smaller amounts of CO, indicating the high ODH activity of the ISA aerogel derived oxide surface. With increasing pulse number and therefore increasing degree of reduction of the surface, the amount of CO and formaldehyde decreased, and after seven pulses, the methanol signal exceeded the aldehyde signal. The bulk V<sub>2</sub>O<sub>5</sub> showed a completely different behavior. At the beginning, V<sub>2</sub>O<sub>5</sub> was less active than the ISA aerogel derived oxide (1st pulse:  $X_{\text{MeOH}} = 77\%$ ) and the conversion decreased to 40% after 8 methanol pulses. Interestingly, the conversion of methanol and therefore the amount of formaldehyde increased again to be 62% after 26 methanol pulses. Afterward, the activity decreased to a degree of conversion of 45% after 50 pulses. This wave-like behavior of the bulk V<sub>2</sub>O<sub>5</sub> clearly indicated the presence and participation of bulk oxygen. During the first pulses, the surface was highly oxidized, leading to a high activity. With an increasing degree of reduction of the surface, fewer active sites were available, leading to a decrease in activity. In a bulk metal oxide system, lattice oxygen can be dynamic and can diffuse from the oxide's bulk to the surface, causing a reoxidation of surface sites, thus regenerating active ODH sites.<sup>47</sup> Nevertheless, this bulk oxygen diffusion has different (lower) time constants compared to the surface processes. Thus, the observed wave-like behavior results. This experiment revealed that the methanol ODH activity of V<sub>2</sub>O<sub>5</sub> at 300 °C was limited by the oxygen bulk dynamic. This was further corroborated by variation of the time between the pulses as given in Supplementary Section 7. Interestingly, the involvement of bulk oxygen and the limitation of the ODH by bulk oxygen dynamics observed for V<sub>2</sub>O<sub>5</sub> was not observed for the ISA aerogel derived oxide.

## 4. CONCLUSION

From the materials characterization and kinetic studies, it can be posited that under ODH conditions the precursor V<sub>4</sub>C<sub>3</sub>T<sub>r</sub> MXene aerogel was partially oxidized, leading to the formation of nanorods consisting of an unusually high degree of active and selective mixture of vanadium oxides, consisting of VO<sub>2</sub>,  $V_6O_{13}$ , and  $V_3O_7$  (and  $V_2O_5$ ). Due to the unique 2D starting material, it was possible to obtain a catalyst where not only the surface consists of mixed valence vanadium oxide "supported" on a fully oxidized bulk but also the full material is in a stable reduced valence state. 48 Very likely, this together with the nanorod arrangement allowed for unprecedented high oxygen mobilities as well as active site numbers, leading to an ultrahigh activity of ISA MXene aerogel derived oxide in alcohol ODH, which is accompanied by high selectivity and stability. The observed lowered desorption energy for the products could also stem from the enrichment of mixed valence states. The MXene starting precursor and aerogel arrangement as well as the softer in situ oxidation were the key to obtain these catalysts. In combination with the large variety of possible MXenes in terms of the choice of metals or metal combinations, this approach of MXene derived oxides paves the way for a completely new field of research toward mixed metal oxide catalysts.

# ASSOCIATED CONTENT

# Supporting Information

The Supporting Information is available free of charge at https://pubs.acs.org/doi/10.1021/acsami.2c22720.

Characterization of  $V_4C_3T_x$  aerogel, ISA aerogel derived oxide, and SSA aerogel derived oxide; catalytic results of reference catalysts; kinetic investigation of ISA aerogel derived oxide and  $V_2O_5$ ; temperature programmed desorption; pulse experiments (PDF)

## AUTHOR INFORMATION

# **Corresponding Author**

Bastian J. M. Etzold — Technical University of Darmstadt, Department of Chemistry, Ernst-Berl-Institut für Technische und Makromolekulare Chemie, 64287 Darmstadt, Germany; orcid.org/0000-0001-6530-4978; Email: bastian.etzold@tu-darmstadt.de

#### **Authors**

Niklas Oefner – Technical University of Darmstadt, Department of Chemistry, Ernst-Berl-Institut für Technische und Makromolekulare Chemie, 64287 Darmstadt, Germany

Christopher E. Shuck — A.J. Drexel Nanomaterials Institute and Department of Materials Science and Engineering, Drexel University, Philadelphia, Pennsylvania 19104, United States; orcid.org/0000-0002-1274-8484

Leon Schumacher – Technical University of Darmstadt, Department of Chemistry, Eduard-Zintl-Institut für Anorganische und Physikalische Chemie, 64287 Darmstadt, Germany

Franziska Heck – Technical University of Darmstadt, Department of Chemistry, Eduard-Zintl-Institut für Anorganische und Physikalische Chemie, 64287 Darmstadt, Germany

Kathrin Hofmann – Technical University of Darmstadt, Department of Chemistry, Eduard-Zintl-Institut für Anorganische und Physikalische Chemie, 64287 Darmstadt, Germany

Jana Schmidpeter – Technical University of Darmstadt, Department of Chemistry, Ernst-Berl-Institut für Technische und Makromolekulare Chemie, 64287 Darmstadt, Germany

Weiqun Li — Department of Mechanical, Materials and Aerospace Engineering, University of Liverpool, Liverpool L69 3GH, United Kingdom

Mounib Bahri – Department of Mechanical, Materials and Aerospace Engineering, University of Liverpool, Liverpool L69 3GH, United Kingdom

B. Layla Mehdi — Department of Mechanical, Materials and Aerospace Engineering, University of Liverpool, Liverpool L69 3GH, United Kingdom; ⊚ orcid.org/0000-0002-8281-9524

Alfons Drochner – Technical University of Darmstadt, Department of Chemistry, Ernst-Berl-Institut für Technische und Makromolekulare Chemie, 64287 Darmstadt, Germany

Barbara Albert – Technical University of Darmstadt, Department of Chemistry, Eduard-Zintl-Institut für Anorganische und Physikalische Chemie, 64287 Darmstadt, Germany

Christian Hess — Technical University of Darmstadt, Department of Chemistry, Eduard-Zintl-Institut für Anorganische und Physikalische Chemie, 64287 Darmstadt, Germany; © orcid.org/0000-0002-4738-7674

Yury Gogotsi — A.J. Drexel Nanomaterials Institute and Department of Materials Science and Engineering, Drexel University, Philadelphia, Pennsylvania 19104, United States; orcid.org/0000-0001-9423-4032

Complete contact information is available at:

## https://pubs.acs.org/10.1021/acsami.2c22720

#### Notes

The authors declare no competing financial interest.

#### ACKNOWLEDGMENTS

The authors thank Karl Kopp for performing the XPS measurements and Miriam Geissler for performing the SEM imaging. N.O., L.S., F.H., K.H., J.S., C.H., and B.J.M.E. acknowledge the funding by the Deutsche Forschungsgemeinschaft (DFG, German Research Foundation) — CRC 1487, "Iron, upgraded!" — Project number 443703006. Development of MXene at Drexel University was supported by the US National Science Foundation grant DMR-2041050.

## REFERENCES

- (1) Herold, F.; Prosch, S.; Oefner, N.; Brunnengräber, K.; Leubner, O.; Hermans, Y.; Hofmann, K.; Drochner, A.; Hofmann, J. P.; Qi, W.; Etzold, B. J. M. Nanoscale Hybrid Amorphous/Graphitic Carbon as Key Towards Next-Generation Carbon-Based Oxidative Dehydrogenation Catalysts. *Angew. Chemie Int. Ed.* **2021**, *60* (11), 5898–5906.
- (2) Zhang, X.; Yan, P.; Xu, J.; Li, F.; Herold, F.; Etzold, B. J. M.; Wang, P.; Su, D. S.; Lin, S.; Qi, W.; Xie, Z. Methanol Conversion on Borocarbonitride Catalysts: Identification and Quantification of Active Sites. *Sci. Adv.* **2020**, *6* (26), 1–10.
- (3) Yan, P.; Zhang, X.; Herold, F.; Li, F.; Dai, X.; Cao, T.; Etzold, B. J. M.; Qi, W. Methanol Oxidative Dehydrogenation and Dehydration on Carbon Nanotubes: Active Sites and Basic Reaction Kinetics. *Catal. Sci. Technol.* **2020**, *10* (15), 4952–4959.
- (4) Oefner, N.; Heck, F.; Dürl, M.; Schumacher, L.; Siddiqui, H. K.; Kramm, U. I.; Hess, C.; Möller, A.; Albert, B.; Etzold, B. J. M. Activity, Selectivity and Initial Degradation of Iron Molybdate in the Oxidative Dehydrogenation of Ethanol. *ChemCatChem* **2022**, *14*, e202101219.
- (5) Reuss, G.; Disteldorf, W.; Gamer, A. O.; Hilt, A. Formaldehyde. In *Ullmann's Encyclopedia of Industrial Chemistry*; Wiley-VCH Verlag GmbH & Co. KGaA: Weinheim, 2012.
- (6) Raun, K. V.; Johannessen, J.; McCormack, K.; Appel, C. C.; Baier, S.; Thorhauge, M.; Høj, M.; Jensen, A. D. Modeling of the Molybdenum Loss in Iron Molybdate Catalyst Pellets for Selective Oxidation of Methanol to Formaldehyde. *Chem. Eng. J.* **2019**, *361* (August 2018), 1285–1295.
- (7) Eckert, M.; Fleischmann, G.; Jira, R.; Bolt, H. M.; Golka, K. Acetaldehyde. In *Ullmann's Encyclopedia of Industrial Chemistry*; Wiley-VCH Verlag GmbH & Co. KGaA: Weinheim, 2012; pp 192–207.
- (8) Pang, J.; Yin, M.; Wu, P.; Li, X.; Li, H.; Zheng, M.; Zhang, T. Advances in Catalytic Dehydrogenation of Ethanol to Acetaldehyde. *Green Chem.* **2021**, 23 (20), 7902–7916.
- (9) Ober, P.; Rogg, S.; Hess, C. Direct Evidence for Active Support Participation in Oxide Catalysis: Multiple Operando Spectroscopy of VO<sub>x</sub>/Ceria. *ACS Catal.* **2020**, *10* (5), 2999–3008.
- (10) Waleska, P.; Rupp, S.; Hess, C. Operando Multiwavelength and Time-Resolved Raman Spectroscopy: Structural Dynamics of a Supported Vanadia Catalyst at Work. *J. Phys. Chem. C* **2018**, *122* (6), 3386–3400.
- (11) Kaichev, V. V.; Chesalov, Y. A.; Saraev, A. A.; Klyushin, A. Y.; Knop-Gericke, A.; Andrushkevich, T. V.; Bukhtiyarov, V. I. Redox Mechanism for Selective Oxidation of Ethanol over Monolayer  $V_2O_5/TiO_2$  Catalysts. *J. Catal.* **2016**, 338, 82–93.
- (12) Beck, B.; Harth, M.; Hamilton, N. G.; Carrero, C.; Uhlrich, J. J.; Trunschke, A.; Shaikhutdinov, S.; Schubert, H.; Freund, H. J.; Schlögl, R.; Sauer, J.; Schomäcker, R. Partial Oxidation of Ethanol on Vanadia Catalysts on Supporting Oxides with Different Redox Properties Compared to Propane. *J. Catal.* **2012**, *296*, 120–131.
- (13) Nair, H.; Gatt, J. E.; Miller, J. T.; Baertsch, C. D. Mechanistic Insights into the Formation of Acetaldehyde and Diethyl Ether from

- Ethanol over Supported VO<sub>x</sub>, MoO<sub>x</sub>, and WO<sub>x</sub> Catalysts. J. Catal. **2011**, 279 (1), 144–154.
- (14) Dutov, V. V.; Mamontov, G. V.; Sobolev, V. I.; Vodyankina, O. V. Silica-Supported Silver-Containing OMS-2 Catalysts for Ethanol Oxidative Dehydrogenation. Catal. Today 2016, 278, 164-173.
- (15) Liu, P.; Hensen, E. J. M. Highly Efficient and Robust Au/ MgCuCr<sub>2</sub>O<sub>4</sub> Catalyst for Gas-Phase Oxidation of Ethanol to Acetaldehyde. J. Am. Chem. Soc. 2013, 135 (38), 14032-14035.
- (16) Malmusi, A.; Velasquez Ochoa, J.; Tabanelli, T.; Basile, F.; Lucarelli, C.; Agnoli, S.; Carraro, F.; Granozzi, G.; Cavani, F. Ethanol Aerobic and Anaerobic Oxidation with FeVO<sub>4</sub> and V<sub>2</sub>O<sub>5</sub> Catalysts. Appl. Catal. A Gen. 2019, 570, 139-147.
- (17) Sobolev, V. I.; Koltunov, K. Y. MoVNbTe Mixed Oxides as Efficient Catalyst for Selective Oxidation of Ethanol to Acetic Acid. ChemCatChem. 2011, 3 (7), 1143-1145.
- (18) Naguib, M.; Kurtoglu, M.; Presser, V.; Lu, J.; Niu, J.; Heon, M.; Hultman, L.; Gogotsi, Y.; Barsoum, M. W. Two-Dimensional Nanocrystals Produced by Exfoliation of Ti<sub>3</sub>AlC<sub>2</sub>. Adv. Mater. 2011, 23 (37), 4248–4253.
- (19) Gogotsi, Y.; Anasori, B. The Rise of MXenes. ACS Nano 2019, 13 (8), 8491-8494.
- (20) Deysher, G.; Shuck, C. E.; Hantanasirisakul, K.; Frey, N. C.; Foucher, A. C.; Maleski, K.; Sarycheva, A.; Shenoy, V. B.; Stach, E. A.; Anasori, B.; Gogotsi, Y. Synthesis of Mo<sub>4</sub>VAlC<sub>4</sub> MAX Phase and Two-Dimensional Mo<sub>4</sub>VC<sub>4</sub> MXene with Five Atomic Layers of Transition Metals. ACS Nano 2020, 14 (1), 204-217.
- (21) VahidMohammadi, A.; Rosen, J.; Gogotsi, Y. The World of Two-Dimensional Carbides and Nitrides (MXenes). Science 2021, 372, 1165-1179.
- (22) Morales-Garciá, A.; Calle-Vallejo, F.; Illas, F. MXenes: New Horizons in Catalysis. ACS Catal. 2020, 10 (22), 13487-13503.
- (23) Rothenberg, G. Catalysis Concepts and Green Applications; WILEY-VCH Verlag GmbH & Co. KFaA: Weinheim, 2008; Vol. 22.
- (24) Zhang, X.; Lei, J.; Wu, D.; Zhao, X.; Jing, Y.; Zhou, Z. A Ti-Anchored Ti<sub>2</sub>CO<sub>2</sub> Monolayer (MXene) as a Single-Atom Catalyst for CO Oxidation. J. Mater. Chem. A 2016, 4 (13), 4871-4876.
- (25) Cheng, C.; Zhang, X.; Yang, Z.; Zhou, Z. Cu<sub>3</sub>-Cluster-Doped Monolayer Mo<sub>2</sub>CO<sub>2</sub> (MXene) as an Electron Reservoir for Catalyzing a CO Oxidation Reaction. ACS Appl. Mater. Interfaces 2018, 10 (38), 32903-32912.
- (26) Cheng, C.; Zhang, X.; Yang, Z.; Hermansson, K. Identification of High-Performance Single-Atom MXenes Catalysts for Low-Temperature CO Oxidation. Adv. Theory Simulations 2019, 2 (8), 1900006.
- (27) Cheng, C.; Zhang, X.; Wang, M.; Wang, S.; Yang, Z. Single Pd Atomic Catalyst on Mo<sub>2</sub>CO<sub>2</sub> Monolayer (MXene): Unusual Activity for CO Oxidation by Trimolecular Eley-Rideal Mechanism. Phys. Chem. Chem. Phys. 2018, 20 (5), 3504-3513.
- (28) Yang, X.; Lu, Z.; Cheng, C.; Wang, Y.; Zhang, X.; Yang, Z.; Lu, W. Identification of Efficient Single-Atom Catalysts Based on V<sub>2</sub>CO<sub>2</sub> MXene by Ab Initio Simulations. J. Phys. Chem. C 2020, 124 (7), 4090-4100.
- (29) Sun, X.; Gao, Y.; Zhao, C.; Deng, S.; Zhong, X.; Zhuang, G.; Wei, Z.; Wang, J. G. Palladium Dimer Supported on Mo<sub>2</sub>CO<sub>2</sub>(MXene) for Direct Methane to Methanol Conversion. Adv. Theory Simulations 2019, 2 (2), 1800158.
- (30) Li, Z.; Yu, L.; Milligan, C.; Ma, T.; Zhou, L.; Cui, Y.; Qi, Z.; Libretto, N.; Xu, B.; Luo, J.; Shi, E.; Wu, Z.; Xin, H.; Delgass, W. N.; Miller, J. T.; Wu, Y. Two-Dimensional Transition Metal Carbides as Supports for Tuning the Chemistry of Catalytic Nanoparticles. Nat. Commun. 2018, 9 (1), 1-8.
- (31) Diao, J.; Hu, M.; Lian, Z.; Li, Z.; Zhang, H.; Huang, F.; Li, B.; Wang, X.; Su, D. S.; Liu, H. Ti<sub>3</sub>C<sub>2</sub>T<sub>x</sub> MXene Catalyzed Ethylbenzene Dehydrogenation: Active Sites and Mechanism Exploration from Both Experimental and Theoretical Aspects. ACS Catal. 2018, 8 (11), 10051-10057.
- (32) Deeva, E. B.; Kurlov, A.; Abdala, P. M.; Lebedev, D.; Kim, S. M.; Gordon, C. P.; Tsoukalou, A.; Fedorov, A.; Müller, C. R. In Situ XANES/XRD Study of the Structural Stability of Two-Dimensional

- Molybdenum Carbide Mo<sub>2</sub>CT<sub>v</sub>: Implications for the Catalytic Activity in the Water-Gas Shift Reaction. Chem. Mater. 2019, 31 (12), 4505-
- (33) Kurlov, A.; Deeva, E. B.; Abdala, P. M.; Lebedev, D.; Tsoukalou, A.; Comas-Vives, A.; Fedorov, A.; Müller, C. R. Exploiting Two-Dimensional Morphology of Molybdenum Oxycarbide to Enable Efficient Catalytic Dry Reforming of Methane. Nat. Commun. 2020, 11 (1), 1-11.
- (34) Thakur, R.; Vahidmohammadi, A.; Smith, J.; Hoffman, M.; Moncada, J.; Beidaghi, M.; Carrero, C. A. Insights into the Genesis of a Selective and Coke-Resistant MXene-Based Catalyst for the Dry Reforming of Methane. ACS Catal. 2020, 10 (9), 5124-5134.
- (35) Zhou, Y.; Li, X.; Chai, Y.; Wu, Z.; Lin, J.; Pan, X.; Han, Y.; Li, L.; Qi, H.; Su, Y.; Kang, L.; Wang, X. Defect-Rich  ${\rm TiO_2}$  in Situ Evolved from MXene for Efficiently Oxidative Dehydrogenation of Ethane. Preprint at https://www.researchsquare.com/article/rs-85939/v1; 2020; DOI: 10.21203/rs.3.rs-85939/v1.
- (36) Ridley, P.; Gallano, C.; Andris, R.; Shuck, C. E.; Gogotsi, Y.; Pomerantseva, E. MXene-Derived Bilayered Vanadium Oxides with Enhanced Stability in Li-Ion Batteries. ACS Appl. Energy Mater. 2020, 3 (11), 10892-10901.
- (37) Ghassemi, H.; Harlow, W.; Mashtalir, O.; Beidaghi, M.; Lukatskaya, M. R.; Gogotsi, Y.; Taheri, M. L. In Situ Environmental Transmission Electron Microscopy Study of Oxidation of Two-Dimensional Ti<sub>3</sub>C<sub>2</sub> and Formation of Carbon-Supported TiO<sub>2</sub>. J. Mater. Chem. A 2014, 2 (35), 14339-14343.
- (38) Su, T.; Peng, R.; Hood, Z. D.; Naguib, M.; Ivanov, I. N.; Keum, J. K.; Qin, Z.; Guo, Z.; Wu, Z. One-Step Synthesis of Nb<sub>2</sub>O<sub>5</sub>/C/Nb<sub>2</sub>C (MXene) Composites and Their Use as Photocatalysts for Hydrogen Evolution. ChemSusChem 2018, 11 (4), 688-699.
- (39) Seredych, M.; Shuck, C. E.; Pinto, D.; Alhabeb, M.; Precetti, E.; Deysher, G.; Anasori, B.; Kurra, N.; Gogotsi, Y. High-Temperature Behavior and Surface Chemistry of Carbide MXenes Studied by Thermal Analysis. Chem. Mater. 2019, 31 (9), 3324-3332.
- (40) Naguib, M.; Mashtalir, O.; Lukatskaya, M. R.; Dyatkin, B.; Zhang, C.; Presser, V.; Gogotsi, Y.; Barsoum, M. W. One-Step Synthesis of Nanocrystalline Transition Metal Oxides on Thin Sheets of Disordered Graphitic Carbon by Oxidation of MXenes. Chem. Commun. 2014, 50 (56), 7420-7423.
- (41) Shuck, C. E.; Ventura-Martinez, K.; Goad, A.; Uzun, S.; Shekhirev, M.; Gogotsi, Y. Safe Synthesis of MAX and MXene: Guidelines to Reduce Risk During Synthesis. ACS Chem. Heal. Saf. 2021, 28 (5), 326-338.
- (42) Vieira Soares, A.P.; Farinha Portela, M.; Kiennemann, A. Iron Molybdates for Selective Oxidation of Methanol: Mo Excess Effects on the Deactivation Behaviour. Catal. Commun. 2001, 2 (5), 159-
- (43) Tran, M. H.; Schäfer, T.; Shahraei, A.; Dürrschnabel, M.; Molina-Luna, L.; Kramm, U. I.; Birkel, C. S. Adding a New Member to the MXene Family: Synthesis, Structure, and Electrocatalytic Activity for the Hydrogen Evolution Reaction of V<sub>4</sub>C<sub>3</sub>T<sub>X</sub>. ACS Appl. Energy Mater. 2018, 1 (8), 3908-3914.
- (44) Shvets, P.; Dikaya, O.; Maksimova, K.; Goikhman, A. A Review of Raman Spectroscopy of Vanadium Oxides. J. Raman Spectrosc. 2019, 50 (8), 1226-1244.
- (45) Oka, Y.; Yao, T.; Yamamoto, N.; Ueda, Y.; Hayashi, A. Phase Transition and V<sup>4+</sup>-V<sup>4+</sup> Pairing in VO<sub>2</sub>(B). J. Solid State Chem. 1993, 105, 271-278.
- (46) Zhang, C.; Yang, Q.; Koughia, C.; Ye, F.; Sanayei, M.; Wen, S. J.; Kasap, S. Characterization of Vanadium Oxide Thin Films with Different Stoichiometry Using Raman Spectroscopy. Thin Solid Films 2016, 620, 64-69.
- (47) Heid, M.; Knoche, S.; Gora, N.; Ohlig, D.; Drochner, A.; Etzold, B. J. M.; Vogel, H. Dynamics of Bulk Oxygen in the Selective Oxidation of Acrolein. ChemCatChem. 2017, 9 (12), 2390-2398.
- (48) Schlögl, R.; Hess, C. Characteristics of Selective Oxidation Reactions. In Nanostructured catalysts: Selective Oxidations; RSC Publishing: Cambridge, 2011.